Journal of Physics: Conference Series **274** (2011) 012071 doi:10.1088/1742-6596/274/1/012071

Stress and deformation in tubular metallic parts of auto seats

[1]Manuel F. M. Costa, [2]José B. Vazquez-Dorrio, [3]Francisco J. Queirós de Melo, [2]Joaquim A. O. Carneiro

[1]Departamento de Física da Universidade do Minho (Portugal)

[2]Universidad de Vigo, EIM, Departamento de Física (Spain)

[3]Department of Mechanical Engineering, University of Aveiro (Portugal)

mfcosta@fisica.uminho.pt

Abstract. In order to assess the structural and material behaviour in particular the deformation and failure in lightweight metallic tubular structural parts of auto seats a pseudo-dynamic procedure was devised. The deformation of circular section tubes subjected to centred transversal force is assessed by rugometric and microtopographic optical inspection.

1. Introduction

In order to assess the structural and material behaviour in particular the deformation and failure in lightweight metallic tubular structural parts of auto seats a pseudo-dynamic procedure was devised. The deformation of circular section tubes subjected to centred transversal force is assessed by rugometric and microtopographic optical inspection can be assessed by measuring strain or the bending of the tubes. Most frequently contact gauges are used in this process [1].

The deformation of the circular section metallic tubes under centred cross wind forces will produce changes in the topographical and microtopographic [2] structure of the pieces and its surfaces, but also significant changes in surface roughness, proportional to the deformation [3,4].

Thus we decide to replace the measuring of deformation using strain sensors that requires time consuming pre-instrumentation (Figure 1) with microtopographic and rugometric inspection of the tube' surface in the area expected to suffer peak deformation (located by finite elements simulation models) (Figure 2).

The inspection was performed using the MICROTOP.06.MFC triangulation based microtopographer developed at the Microtopography' laboratory of the Department of Physics of the University of the Minho. Bending radius can me directly measured. For stronger deformations bending radius becomes unreliable and full topographic inspection must be performed. Statistical roughness characterization parameters are calculated.

Rugometric characterization must be performed by calculation of suitable ISO statistical parameters (ISO 4287, ISO 12085 and ISO 13565-2). Among those, average roughness, Ra, is of generalized use and straightforward interpretation. Also in this context it is of interest revealing a good correlation with the mechanical parameters that characterise of the induced deformation.

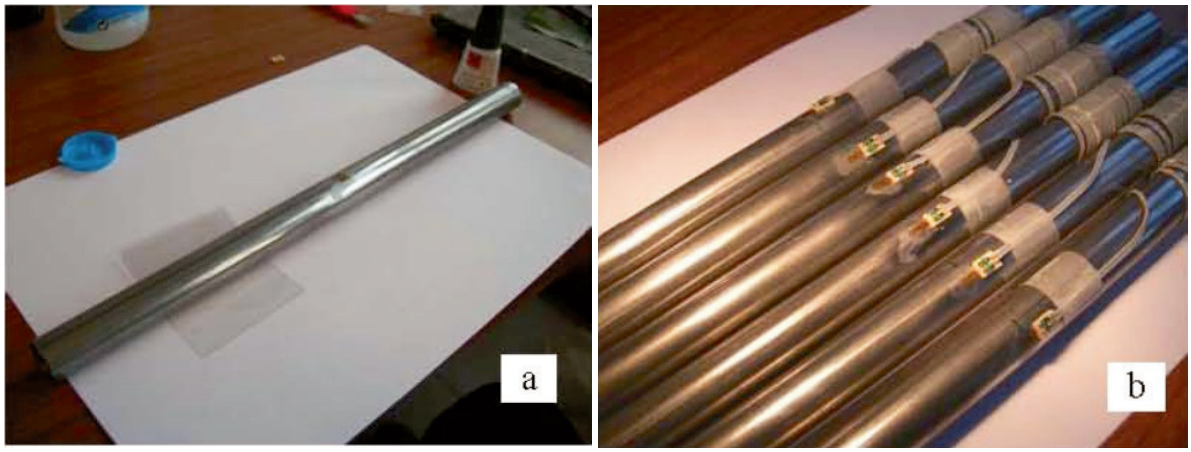

Figure 1. Steel tubes used in the construction of car seats (a) during the process of application of the strain gauges (b) for measurement of tube bending (Figure 2).

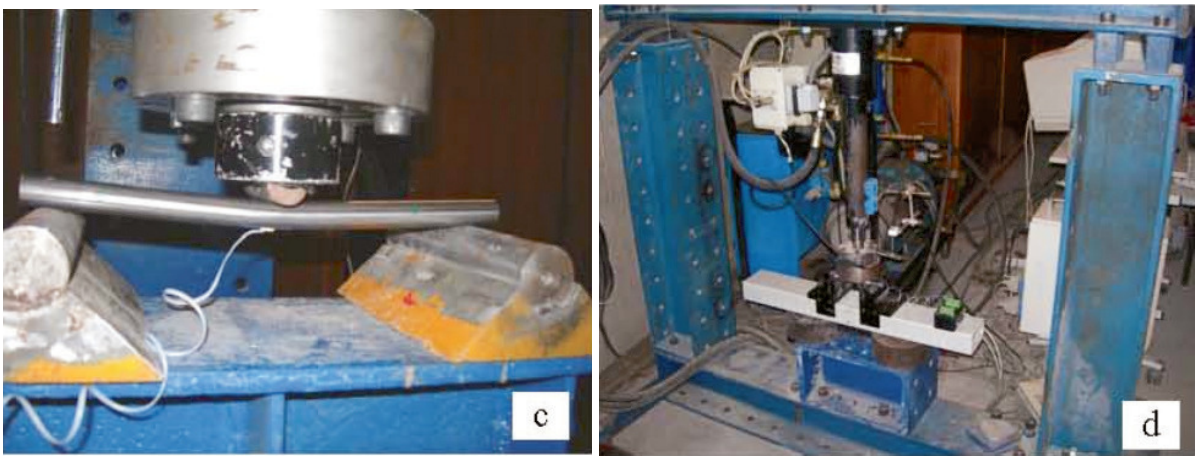

Figure 2. Car seat' steel tubes subject to bending tests.

The particular shape of the samples to be inspected (more or less deformed cylinders) make it mandatory to first remove the factor of form of the relief by nonlinear least square fitting using the Levenberg-Marquardt algorithm.

The separation of roughness regimes (ISO 1386) must then be performed according to ISO rules (ISO 13565-1 of 1996) applying Gaussian filtering at the cut-off chosen according to norm ISO 4288.

In order to avoid differences in roughness of the tubes to be used in the test we adjusted the roughness of the surfaces texturing the tube surfaces (around the bending area) by sand blasting.

2. Structural and Material Behaviour of Parts of Car' Seats

In order to study the resistance of car seats is extreme stress situations extensive testing is needed. The structural and material behaviour of the tubular parts of car seats was addressed in this study. Among the different studies possible a dynamic bending test setup was built to simulate the car seat deformation as sketched in figure 3 [5,6]. In figure 4 the system' technical drawing is presented and in the pictures on figure 5 the actual system is shown.

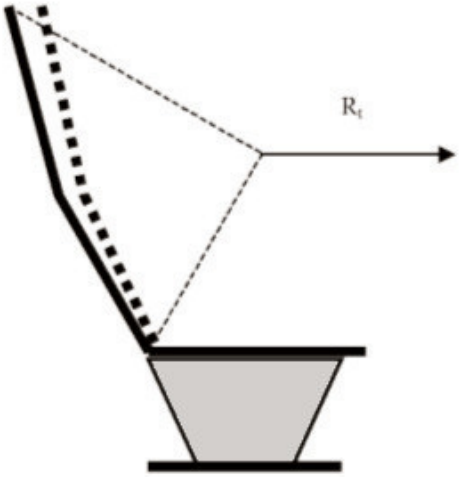

Figure 3. Deformation of a car seat considered in this work.

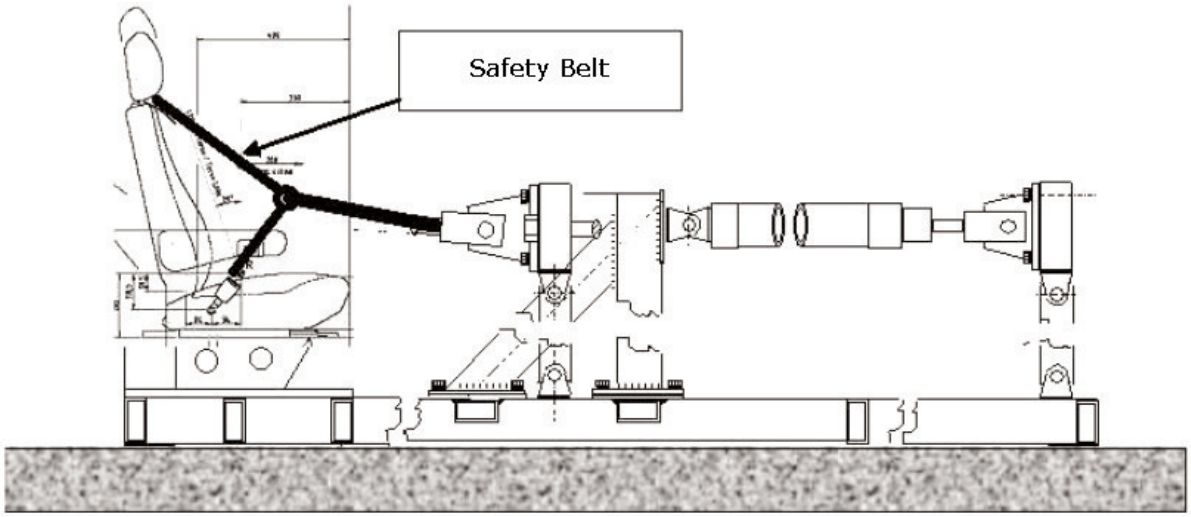

Figure 4. Technical drawing of the dynamic test system setup designed to study the behaviour of car seats subjected to frontal bending.

The strategy adopted in the implementation of the pseudo-dynamic method for the dynamic analysis of the bending of a car seat consisted on first performing a finite elements modelling of the process to characterize the impulsive load curve adequately and therefore to be able to foresee the localization of the regions of the test tube where it would be foreseeable to occur the maximum deformations. Bending tests were performed in cylindrical steel tubes to measure the amplitude of deformations and roughness changes in the tubes surfaces in the bended regions. Finally tests woth actual car seats were performed with the dynamic test system (figure 5).

Figure 5. Views of the actual dynamic test system of car seat deformations.

In order to measure the relation between the applied deforming force and the bending deformation of the car tubes and the roughness of its surface a bench test was devised. In figure 6 is shown a schematic representation of the deformation test geometry. With this geometry the tube' bending displacement at mid tube will be:

$$\delta = \frac{PL^3}{48EI} + \frac{P/2 \times L}{GAk} \qquad (1)$$

were δ (or y) is the vertical displacement at mid tube. The second term of equation 1 results from the deformation energy (theorem of *Castigliano*).

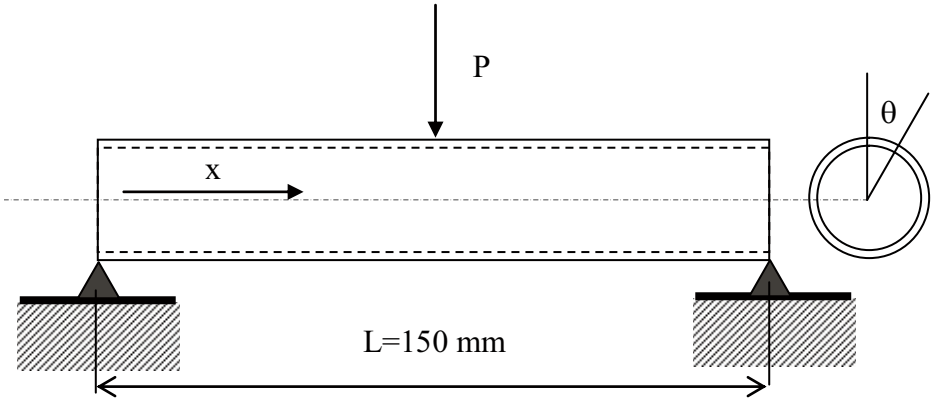

Figure 6. Schematic diagram of the bending test.

Assuming that the tube has a Reissner behaviour, i. e., the transversal deformation appears as:

$$\gamma_{x\theta} = \frac{\partial u}{r\partial\theta} + \frac{\partial v}{\partial x} \tag{2}$$

and that *W* is the tube transversal displacement; β is the rotation angle due to the flexion; *u* the displacement along x; v the displacement along θ; and θ the angle of position in the point of deformation resulting on the relations:

$$\begin{aligned} u &= -r\cos\theta \times \beta \\ v &= -W\sin\theta \end{aligned} \tag{3}$$

the breaking, cut-off, deformation will be:

$$\gamma_{x\theta} = \frac{\partial u}{r\partial\theta} + \frac{\partial v}{\partial x} = -\sin\theta\left(\frac{\partial W}{\partial x} - \beta\right) \tag{4}$$

The deformation energy in breaking deformation for this particular tube shape requires a correction factor k=0.5 (for a rectangular section tube k would equal 5/6). Thus for our tubes r=5mm (radius), t=1mm (thickness) e L=100mm (length), and an elasticity module of E=210GPa (steel), the vertical displacement at mid tube δ is:

$$\delta = (2.92E - 4)\, P \tag{5}$$

If the contribution of the cutting resistance is ignored equation 5 becomes:

$$\delta = 2.52E - 4 \tag{6}$$

Considering that the ovalization of the tubes presents only two forms 2θ e 3θ, the depth deformation in the support points and at the point of application of the charge is:

$$a = \frac{2.5\,Pr^3}{9\pi DL} \tag{7}$$

were P is the radial force applied on the surface of the tube and d:

$$D = \frac{Et^3}{12(1-\nu^2)} \tag{8}$$

Knowing that there are 3 radial forces over the tube (force P e two reactions P/2), the total deformation due to ovalization is, in approximation:

$$a_{total} = \frac{5\,Pr^3}{9\pi D(L/2)} \tag{9}$$

Therefore the total deformation is:

$$\delta = \frac{PL^3}{48EI} + \frac{P/2 \times L}{GAk} + \frac{5\,Pr^3}{9\pi D(L/2)} \tag{10}$$

In the elastic regime the elasticity module E can obtained differentiating equation 10 in order to δ:

$$E = \left[\frac{L^3}{48\,I} + \frac{(1+\upsilon)\,L}{A\,k} + \frac{120\,r^3(1-\upsilon^2)}{9\pi\,L\,t^3}\right]\left(\frac{dP}{d\delta}\right) \tag{11}$$

were $\left(\frac{dP}{d\delta}\right)$ can be obtained from linear fitting on the curve of charge of the deformation tests performed.

In order to avoid differences in roughness of the tubes to be used in the test we adjusted the roughness of the surfaces texturing the tube surfaces (around the bending area) by sand blasting.

3. Structural and Material Behaviour of Parts of Car' Seats

A range of optical profilometers and microtopographers was developed at the Physics Department of the Universidade do Minho aiming different applications improved and adapted according to particular inspection needs [2, 7-12]. The main system, the MICROTOP.03.MFC, is intended for general use on the inspection of rough surfaces (both 2D and 3D); the MICROTOP.PL1.MFC system is a simplified version used on the inspection of polymer pieces and materials [11]; a simple hand held version [2]; and the version MICROTOP.06.MFC adapted by incorporation of an angle resolved scattering structure with height resolution measuring capabilities down to the nanometer range is the latest and more versatile version.

Discreet active triangulation [2, 7, 13] is the method employed. Essentially in this kind of sensors a beam of light shines on the sample at some angle and the reflected light is collected at another angle.

The general triangulation geometry is sketched below. Of particular interest are the situations: where the observation angle equals the incidence one, and we will be looking at the specular reflection achieving high height resolutions, on the nanometer range; and, when either normal observation (our choice as explained elsewhere [7]) or incidence is settled resulting on a geometry most suitable for the inspection of rougher surfaces, the most frequent case in industry. The relation between the lateral spots' displacement and height is easily established.

The former system, the MICROTOP.03.MFC, was based on a method involving optical active triangulation (figure 7) with oblique incidence and normal observation, and mechanical sample's scanning. Now another triangulation arm is incorporated on the sensor's head allowing specular triangulation with resolutions down to the nanometer range. Furthermore when using a linescan scan camera with 2048 elements, pitch 13μm, the roughness of smoother samples can be measured by an angular resolved scattering approach [14-15]. If on the specular observation arm a differential photodiode is employed resolution of a few nanometer are achieved on the inspection of smooth surfaces. A CCD camera with a coaxial illuminator allows 2D images to be acquired and processed [16]. In the MIROTOPO.06.MFC the method was extended by incorporating angle resolved scattering methods. The setup and the inspection process are briefly described next referring to figure 8.

The surface to be inspected is scanned by one oblique light beam. Different light sources are available and can be easily interchanged: two HeNe lasers at 632.8 and 534nm, and, one Xe white light sources. The incident light is collimated and focused. A small, diffraction limited, bright spot is thus projected onto the sample. The bright spot is imaged both perpendicularly and specularly onto electronic photosensitive detection systems in order to assess its lateral position. As sensors several options are available to be chosen according to the required application: one 2048 pixels Fairchild CCD linear array on the specular arm and a Reticon line scan camera; one PSD; and a differential detector. The area of the surface to be inspected is scanned point by point by the "sensor's tip" (the light beam focused onto the surface). The highest system's robustness was sought. Also a high lateral positioning resolution and accuracy should be achieved. Thus both the incidence arm and observation arms of the sensor are kept fixed. In order to perform the sample's scanning it will be moved by means of a precision XY displacement table driven by precision step motors. Piezo-driven motors allow positioning with nanometer resolution in a 1.5mm range.

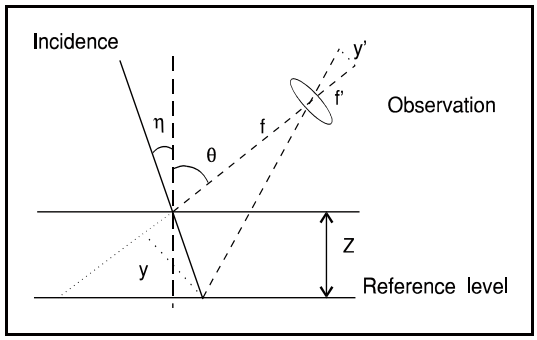

The relation between the measured value (y') and height (Z) comes:

$$y' = M\frac{Z\sin(\eta+\theta)}{\cos\eta+(Z/f)\cot(\eta+\theta)}$$

where M=f/f' is the optical magnification in the observation arm, f and f' are the focal lengths of the observation optics, η the incidence angle and θ the observation one.

Figure 7. A sketch of the general triangulation geometry.

At each scanning point, on a rectangular array separated by distances down to 1.25 μm, the lateral spot's position in both sensors is obtained and registered. The spot's shift on both detectors' planes, between consecutive scan positions is directly related with the height differences between those surface' inspected points. In the "specular" of the system the detector can be positioned (just introducing an adapter) tilted relative to the observation optics in order to increase the depth range of the sensor (Schleimpflug' condition). Employing the linear arrays both arms are on a confocal arrangement allowing the best resolution.

The incidence set-up comprises apart from the light source a neutral density variable filter, a motorised beam steering system, a spatial filter and focusing optics. The change on the incidence angle is made synchronised with the change of the observation angle on the specular arm. A vertical movement precision stage endowed of computer controlled motion provided by a reliable accurate DC encoder with high positioning repeatability and resolution is used refocusing of the observation optical system but especially for calibration of both arms of the sensor. In order to resolve shaded areas and mutual reflections, a high precision rotational stage is used allowing easy change to opposite light

incidence. Often the faces of the surface to be analysed are not parallel or simply the surface to be inspected does not lie horizontally. In order to maintain the best height resolution a tilt table was incorporated to the samples' positioning system. Furthermore it may allow the inspection of 3D objects or surfaces with pronounced holes of it, for instance.

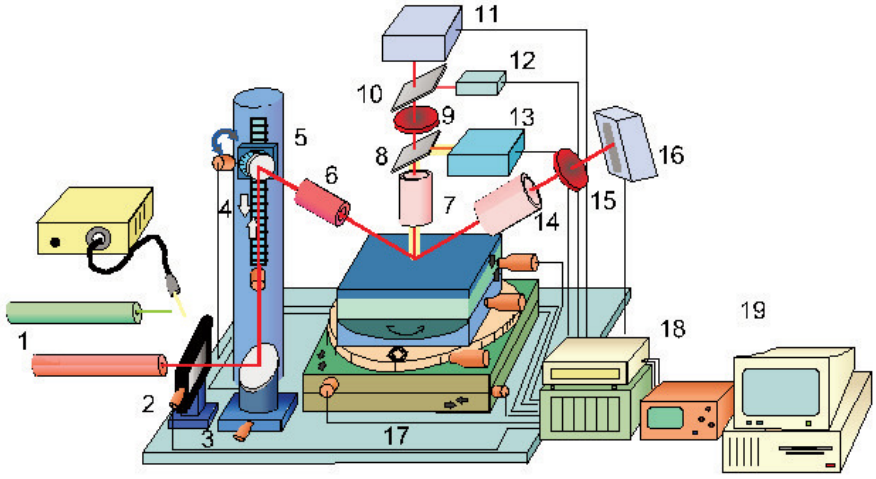

Figure 8. 1. Interchangeable light sources; 2: Vibration isolation stand; 3. Neutral density filter; 4. Beam steering system; 5. Incidence angle control motorised system; 6. Incidence optics; 7. Normal observation optics; 8. and 9. Beam splitters; 10. Interference filter; 11. Normal photosensitive detection system; 12. Photodetector; 13. Video camera and illuminator; 14. Specular observation optics; 15. Interference filter; 16. Specular photosensitive detection system 17. Sample support and motorised positioning system; 18. Data acquisition and control system; 19. Microcomputer.

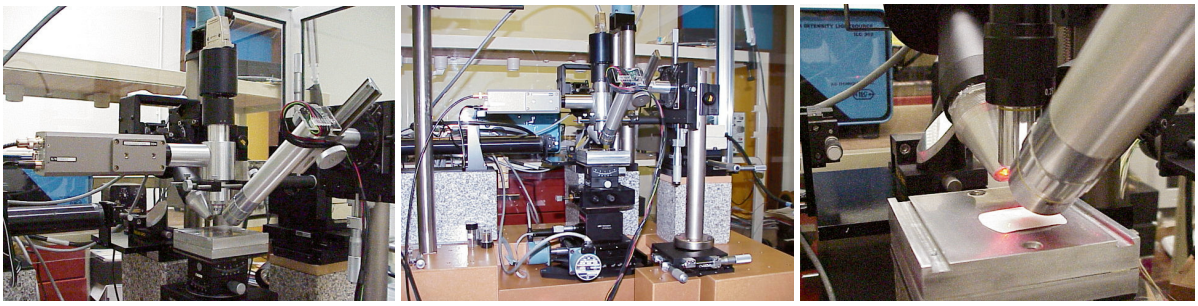

Figure 9. A few pictures of the MICROTOP.06.MFC system.

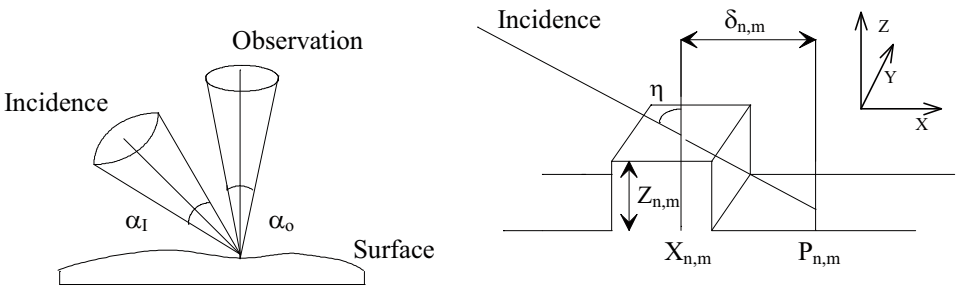

Figure 10. The surface's relief inspection system we implemented is based on the geometry sketched above. The intersection of an oblique light beam with an opaque surface creates on it a bright spot whose lateral position depends on the surface height.

The observation optical systems are formed by microscope objectives chosen according to the characteristics of the surface's relief. In both sensor' arms the objectives can be independently focused. They will be used to image the light spot onto the opto-electronic photosensitive detection systems. Both the "normal" and the "specular" sensors' arms are attached to a XYZ precision displacement table for finer adjustments. A 2D CCD camera was attached to the system allowing the capture of bidimensional colour images of the scanned area for matching and improved visualisation aid. Projection of the actual 2D image onto the 3D map is being studied at the moment. In order to cope with different requirement different photosensitive systems are available and all are interchangeable. A personal microcomputer acquires the data and takes control of the whole inspection process and result's presentation. At the end of the inspection process we may have just one but typically will have two sets of data one for each sensor's arm. Data processing is independently performed and two sets of parameters and functions are obtained by triangulation and scattering analysis. The correlation of the sets of data is investigated. Comparison and matching is performed in order to obtain just one the best set of reliable and accurate data.

From figure 10 and the above considerations is easy to see that the set of 3D co-ordinates obtained by the system is:

$$\begin{aligned} X_{n,m} &= n\Delta - \delta_{n,m} ; \\ Y_{n,m} &= m\Phi ; \\ Z_{n,m} &= (\delta_{n,m}/M) \cot \eta , \end{aligned} \qquad (11)$$

where η is the incidence angle, Δ the sweep increment in the direction of the plane of incidence (X) and Φ in the perpendicular one, M the magnification of the observation system placed above, perpendicularly, to the surface, and $\delta_{n,m}$ the spot shift (on the X direction), regarding a reference position $P_{n,m}$, at the scan position (X_n, Y_m).

The type, and its relief characteristic in the three dimensions, of the surface under inspection condition the overall performance of this method in addition to its particular implementation. The depth resolution will be conditioned by the speckle effects, as we use an HeNe laser as light source, and it will be essentially limited by the Rayleigh limit modified upon the system's particular configuration. Referring to figure 10:

$$Z_{min} = (\lambda/\sin \alpha_o) \cot \eta \qquad (12)$$

The dynamic range as well as the lateral resolution depends upon the system's configuration and the later will be defined by the maximum scanning resolution and the spot's size and configuration.

In order to overcome the triangulation's inherent problem of shadowing and mutual reflection we scan the sample consecutively with two opposite angles η and $-\eta$). The results are then matched and the final set of 3D coordinates is obtained. The reproduction of surface's relief structure can then be performed in different ways and statistical surface characterization parameters are computed.

4. Experimental results

In the following table and graphs we will presents the results of the microtopographic inspection of the tubes subjected to the bending tests correlating the average roughness, Ra, obtained as explained at chapter 1 with other meaningful test parameters as strain and stress. In table 1 a set of four reference strain/stress/average roughness values is presented. From those values we plot in figure 11 the relation between average roughness and strain including in the plot uncertainty bars. In figure 12 the relation between the applied force and the tube deformation is shown. The direct proportionality between strain and deformation is plotted in figure 13 In next figure we plot the dependence of average roughness and stress on strain and on figure 15 the dependence on stress of the average roughness and strain is shown. For the steel tubes used the average value of the modulus of elasticity is of 209.3 GPa and the average value of elastic tension equals 50.3 MPa.

Table 1. Relation between roughness and strain and stress for 4 reference test steel tubes

STRAIN (μm/m)	STRESS (MPa)	Average Roughness (μm)
4700	184	2.94
3720	171	2.38
2270	153	1.95
1110	129	1.79

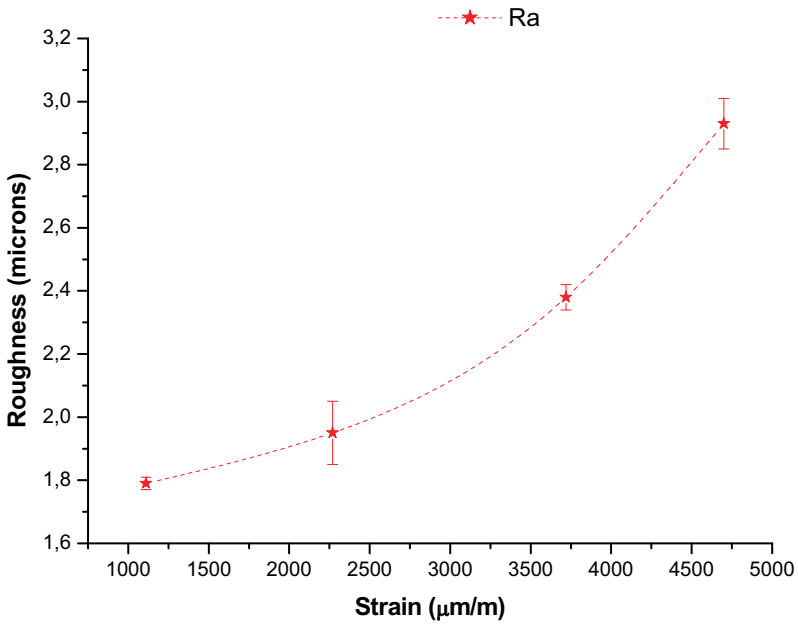

Figure 11. Relation between average roughness and strain (Ra uncertainty bars included).

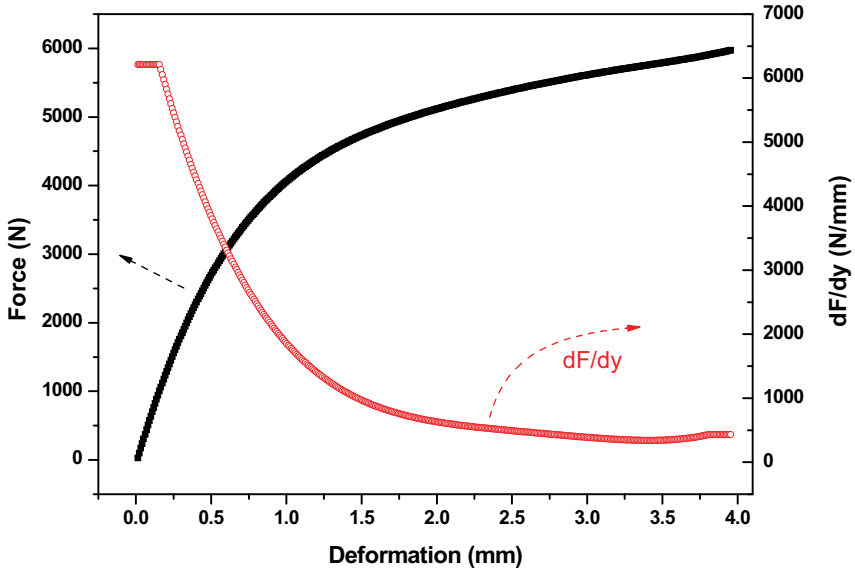

Figure 12. Relation between applied force and tube deformation.

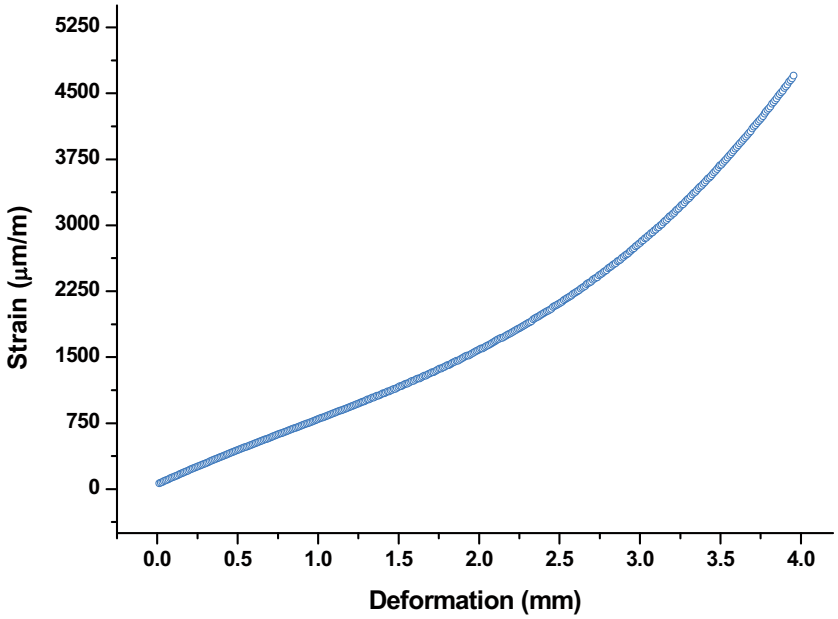

Figure 13. Relation between strain and deformation in the car seat steel tubes bending tests.

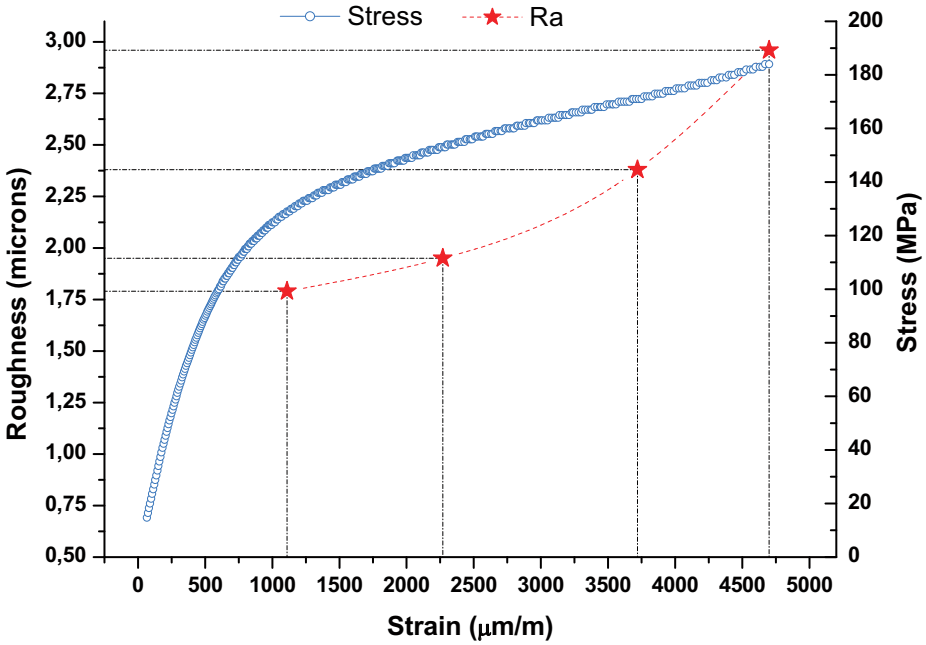

Figure 14. Dependence of average roughness and stress on strain.

In order to avoid differences in roughness of the tubes to be used in the test we adjusted the roughness of the surfaces texturing the tube surfaces (around the bending area) by sand blasting.

5. Conclusion

When performing the assessment of deformation and failure in lightweight metallic tubular structural parts of auto seats by optical microtopographic inspection of deformed tubes, a correlation between strain and stress and surface's average roughness was found.

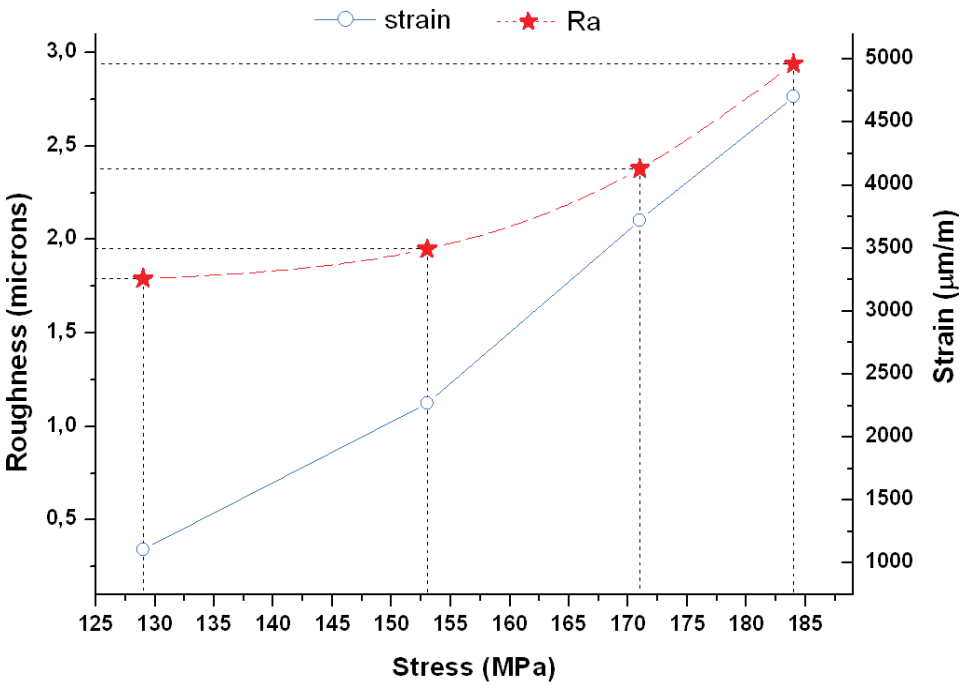

Figure 15. Dependence on stress of the average roughness and strain.

References

[1] Alexander J and Gunasekera J S 1991 *Strength of Materials* (Ellis Hordood, Chichester, UK)

[2] Costa M F M 1996 Surface Inspection by an Optical Triangulation Method *Optical Engineering* **35** 2743-2747

[3] Den Hartog J P 1987 *Advanced Strength of Materials* (Dover Publications, New York)

[4] Timoshenko S P and Goodier J N 1970 *Theory of Elasticity* (McGraw-Hill, Singapore)

[5] Carneiro J O, de Melo F Q, Rodrigues J , H. Lopes H and Teixeira V 2005 Steel Tube Bending *International Journal of Pressure Vessels and Piping* **82** 593-601

[6] de Melo F Q and de Castro P T 1992 Finite Elements Modelling of Hard Pipes *Computers & Structures* **43** 787-794

[7] Costa M F M and Almeida J 1993 System of Optical Non Contact Microtopography *Applied Optics* **32** 4860-4863

[8] Costa M F M and Pinho V 2001 Microtopographic Inspection of Thermoplastic Rubber Shoe Sole. The influence of surface roughness on sole to leather gluing *NDT&E Int. Journal* **34** 11-16

[9] Rocha J G, Schabmueller C G J, Ramos N F, Lanceros-Mendez S, Costa M F M; Evans A G R; Wolffenbuttel R F and Correia J 2003 X-ray detector based on a bulk micromachined photodiode combined with a scintillating crystal *J. Micromech. Microeng.* **13** S45-S50

[10] Pacheco M C L, Gallegos E R, Zapata A J P, Cherit J D and Costa M F M 2005 Implementation and analysis of relief patterns of the surface of benign and malignant lesions of the skin by microtopography *Phys. Med. Biol.***50** 5535-5543

[11] Oliveira M J, Brito A M, Costa M C and Costa M F 2006 Gloss and surface topography of ABS: A study on the influence of the injection moulding parameters *Polymer Eng. and Sci.* **46** 1394-1401

[12] Teixeira, V, Sousa E, Costa M F M, Nunes C, Rosa L, Carvalho M J, Collares-Pereira M, Roman E and Gago J 2001 Spectrally selective composite coatings of Cr-Cr_2O_3, and Mo-Al_2O_3 for solar energy applications *Thin Solid Films* **392** 320-326

[13] Tanwar L S and Kunzmann H 1984 An electro-optical sensor for microdisplacement measurement and control *J. Phys. E: Sci. Instrum.* **17** 864-868

[14] Church E L ,Jenkison H A and Zavada J M1977 Measurement of the finish of diamond turned metal surfaces by differential light scattering *Opt. Eng.* **16** 360-374

[15] Church E L, Jenkison H A and Zavada J M 1979 Relationship between surface scattering and microtopographic features *Opt. Eng.* **18** 125-136